



Cite this: *RSC Adv.*, 2019, 9, 14391

# Enhanced photocatalytic reduction of CO<sub>2</sub> to CO over BiOBr assisted by phenolic resin-based activated carbon spheres†

Kangli Liu,<sup>a</sup> Xiaochao Zhang,<sup>b</sup> <sup>\*,a</sup> Changming Zhang,<sup>a</sup> Guangmin Ren,<sup>a</sup> Zhanfeng Zheng,<sup>b</sup> <sup>b</sup> Zhiping Lv<sup>\*,a</sup> and Caimei Fan<sup>\*,a</sup>

Photocatalytic reduction of CO<sub>2</sub> using solar energy to decrease CO<sub>2</sub> emission is a promising clean renewable fuel production technology. Recently, Bi-based semiconductors with excellent photocatalytic activity and carbon-based carriers with large specific surface areas and strong CO<sub>2</sub> adsorption capacity have attracted extensive attention. In this study, activated carbon spheres (ACSs) were obtained via carbonization and steam activation of phenolic resin-based carbon spheres at 850 °C synthesized by suspension polymerization. Then, the BiOBr/ACSs sample was successfully prepared via a simple impregnation method. The as-prepared samples were characterized by XRD, SEM, EDX, DRS, PL, EIS, XPS, BET, CO<sub>2</sub> adsorption isotherm and CO<sub>2</sub>-TPD. The BiOBr and BiOBr/ACSs samples exhibited high CO selectivity for photocatalytic CO<sub>2</sub> reduction, and BiOBr/ACSs achieved a rather higher photocatalytic activity (23.74 μmol g<sup>-1</sup> h<sup>-1</sup>) than BiOBr (2.39 μmol g<sup>-1</sup> h<sup>-1</sup>) under simulated sunlight irradiation. Moreover, the analysis of the obtained results indicates that in this photocatalyst system, due to their higher micropore surface area and larger micropore volume, ACSs provide enough physical adsorption sites for CO<sub>2</sub> adsorption, and the intrinsic structure of ACSs can offer effective electron transfer ability for a fast and efficient separation of photo-induced electron-hole pairs. Finally, a possible enhanced photocatalytic mechanism of BiOBr/ACSs was investigated and proposed. Our findings should provide new and important research ideas for the construction of highly efficient photocatalyst systems for the reduction of CO<sub>2</sub> to solar fuels and chemicals.

Received 21st February 2019

Accepted 1st April 2019

DOI: 10.1039/c9ra01329f

rsc.li/rsc-advances

## 1. Introduction

With the rapid development of industrial economy, the global environmental pollution and energy crisis have become extremely significant challenges that humans are facing in the short-term.<sup>1</sup> More importantly, the heavy reliance of economic development on the fossil fuel energy will bring about more than 30.4 Gt a<sup>-1</sup> of CO<sub>2</sub> emissions into the atmosphere,<sup>2</sup> and the CO<sub>2</sub> emissions will probably increase up to 43 Gt a<sup>-1</sup> by 2035 without factitious CO<sub>2</sub> conversion utilization. Moreover, CO<sub>2</sub> has been considered as a dominating factor for the anthropogenic climate change to cause the “Greenhouse Effect”; therefore, it is necessary to find out suitable ways for the maximum utilization of CO<sub>2</sub>.<sup>3,4</sup> At present, solar photocatalytic technology, as a great potential way to solve the abovementioned problem,

has received significant attentions for the reduction of CO<sub>2</sub> to useful high-energy fuels (*e.g.* CO, CH<sub>3</sub>OH, CH<sub>4</sub>, HCOOH, *etc.*).<sup>5–10</sup> Among them, CO, as a crucial feedstock in the d-metal-catalyzed Fischer-Tropsch synthetic processes, possesses a significant fuel value ( $\Delta_c H = -283.0$  kJ mol<sup>-1</sup>) and is also easily converted to CH<sub>3</sub>OH; therefore, it is attracting significant interest from researchers.<sup>11</sup> Most importantly, it is imperative to find a suitable and promising photocatalyst system with high selectivity and activity for CO<sub>2</sub> reduction under the action of solar light.

BiOBr, as one of the Bi-based semiconductors with several advantages, including earth abundance, stability, economy and non-toxicity, exhibits a unique layered structure, excellent electrical and optical properties as well as a suitable indirect band gap (~2.7 eV) to endow effective photocatalytic activity and stability.<sup>12–17</sup> It was believed that the Bi 6s and O 2p states could form a large number of dispersed hybridized valence bands, which facilitated the migration and oxidation of photo-generated holes; this induced the efficient separation of photo-generated electron-hole (e<sup>-</sup>-h<sup>+</sup>) pairs and then improved the photocatalytic efficiency.<sup>18</sup> In 2016, Ye *et al.* found that the as-prepared BiOBr sample with ultrathin thickness and a Bi-rich structure could convert CO<sub>2</sub> to CO (2.67 μmol g<sup>-1</sup> h<sup>-1</sup>) and

<sup>a</sup>College of Chemistry and Chemical Engineering, Taiyuan University of Technology, Taiyuan 030024, PR China. E-mail: zhangxiaochao@tyut.edu.cn; Fax: +86-351-6018554; Tel: +86-155-03477962

<sup>b</sup>State Key Laboratory of Coal Conversion, Institute of Coal Chemistry, Chinese Academy of Sciences, China

† Electronic supplementary information (ESI) available. See DOI: 10.1039/c9ra01329f

$\text{CH}_4$  ( $0.16 \mu\text{mol g}^{-1} \text{h}^{-1}$ ).<sup>19</sup> After this, in 2017, they reported that {001}-dominated BiOBr nanosheets showed 100% selectivity for the conversion of  $\text{CO}_2$  to CO and the highest CO yield of  $4.45 \mu\text{mol g}^{-1} \text{h}^{-1}$  under simulated sunlight irradiation.<sup>20</sup> Most importantly, in 2018, Xie *et al.* synthesized defect-engineered BiOBr atomic layers with a rather high CO yield ( $87.4 \mu\text{mol g}^{-1} \text{h}^{-1}$ ) for the photocatalytic reduction of  $\text{CO}_2$  under visible light-driven irradiation.<sup>21</sup> These remarkable findings well confirmed that BiOBr, as a promising new-type of  $\text{CO}_2$  reduction material, could be responsible for the excellent selectivity and activity of the photocatalytic reduction of  $\text{CO}_2$  to CO. As is known, the separation efficiency of photogenerated  $\text{e}^-$ - $\text{h}^+$  pairs and the adsorption performance of  $\text{CO}_2$  on the catalyst surface have been two significant and crucial factors for the photocatalytic reduction of  $\text{CO}_2$ .<sup>4,22–24</sup> However, for a single BiOBr photocatalyst, the low separation efficiency of the electron-hole pairs and the weak  $\text{CO}_2$  adsorption capacity limit its development and applications in the photocatalytic reduction of  $\text{CO}_2$ . Therefore, it is urgent to construct an ideal photocatalyst system with excellent light absorption, efficient separation of photo-generated  $\text{e}^-$ - $\text{h}^+$  pairs and high  $\text{CO}_2$  adsorption capacity.<sup>25</sup>

According to abovementioned problems, the selection of materials with higher adsorption capacity, larger specific surface area and stronger charge transfer ability to be loaded onto high-efficiency photocatalysts should be a very significant and interesting issue in the research and development of photocatalytic  $\text{CO}_2$  reduction; in most of the studies, it has been found that carbon-based carriers (such as activated carbon,<sup>26</sup> carbon nanotubes,<sup>27</sup> graphene,<sup>28</sup> and carbon nanodots<sup>29</sup>) meet these requirements due to their unique electronic structures, stable chemical structures, large specific surface areas, strong adsorption capacities, high thermal conductivity and electron mobilities.<sup>30</sup> Especially, activated carbon spheres (ACSs) with excellent electron transfer capability, suitable sphere-type structure and size, high loading density and mechanical strength, have attracted widespread attention as a kind of promising and valuable adsorbent for hazardous materials in the liquid and gas phases as well as catalyst supports. For example, Liu *et al.* found that micrometer-sized carbon spheres, rich in O-containing functional groups, exhibited a remarkably enhanced adsorption capacity for  $\text{Cr}(\text{vi})$ ,  $0.4834 \text{ mmol g}^{-1}$ , about 4 times that of unmodified AC.<sup>31</sup> Wickramaratne *et al.* prepared a series of activated carbon spheres (ACSs) through the carbonization of phenolic resin spheres using the one-pot modified Stöber and  $\text{CO}_2$  activation method, which exhibited high surface areas (from  $730$  to  $2930 \text{ m}^2 \text{ g}^{-1}$ ) and  $\text{CO}_2$  adsorption capacities at 1 bar ( $4.55$  and  $8.05 \text{ mmol g}^{-1}$ , at  $25^\circ\text{C}$  and  $0^\circ\text{C}$ , respectively).<sup>32</sup> Moreover, Rivera-Utrilla *et al.* and Ao *et al.* synthesized  $\text{TiO}_2$ -AC<sup>33</sup> and BiOBr-AC<sup>26</sup> photocatalysts, respectively, with greatly improved photocatalytic performances owing to the higher BET surface area of the AC support with strong adsorption capacity for pollutants and significant influence on the optical absorption capacity and crystal size of the catalysts. Therefore, due to their high specific surface areas and strong  $\text{CO}_2$  adsorption capacity, ACSs can become rather ideal carriers to support high-efficiency photocatalysts to effectively enhance the performance of photocatalytic  $\text{CO}_2$  reduction.

Among them, phenolic resins have been considered as promising polymer precursor materials to produce ACSs with high surface areas because of their low inorganic impurity and negligible ash contents. In our study, a new method is reported for the preparation of ACSs. At first, phenolic resin-based spheres were synthesized by suspension polymerization using *m*-cresol and formaldehyde as precursor materials and adding ethylene glycol or poly(ethylene glycol) as an additive; then, the millimeter-sized ACSs with high specific surface area were prepared by the steam activation method. Subsequently, a layer of BiOBr was uniformly loaded on the ACSs surface using a simple impregnation method. The phase structure, morphology, elemental analysis, optical absorption characteristics, specific surface areas and  $\text{CO}_2$  adsorption ability of the as-prepared BiOBr/ACSs were analyzed by XRD, SEM, EDX, XPS, DRS, PL, EIS, BET,  $\text{CO}_2$  adsorption isotherm and  $\text{CO}_2$ -TPD. In addition, the correlative performances of photocatalytic  $\text{CO}_2$  reduction were evaluated under simulated sunlight irradiation. Finally, the photocatalytic mechanism of action of the BiOBr/ACSs sample has been investigated and proposed; the results obtained herein should provide new and important research ideas and great guiding significance for the construction of highly-efficient photocatalyst systems for photocatalytic  $\text{CO}_2$  reduction.

## 2. Experimental

### 2.1 Chemicals

Bismuth nitrate pentahydrate ( $\text{Bi}(\text{NO}_3)_3 \cdot 5\text{H}_2\text{O}$ ) and potassium bromide (KBr) were purchased from Tianjin Sinopharm Chemical Reagent (Co. Ltd.) and Tianjin Zhiyuan Reagent (Co. Ltd.), respectively. *m*-Cresol was obtained from Aladdin. Formaldehyde, ethylene glycol (EG), and hexamethylenetetramine were provided by Tianjin Kemiou Chemical Reagent (Co. Ltd.). Triethylamine and polyvinyl alcohol were provided by Tianjin Fangde Technology (Co. Ltd.) and Shanxi Sanwei Group (Co. Ltd.). All reagents were of analytical grade. Deionized water was used throughout this study.

### 2.2 Preparation

**BiOBr.** In a typical synthesis,  $0.01 \text{ mmol}$  of  $\text{Bi}(\text{NO}_3)_3 \cdot 5\text{H}_2\text{O}$  was dissolved in  $40 \text{ mL}$  of ethylene glycol (EG) at  $50^\circ\text{C}$ , and  $0.01 \text{ mmol}$  of KBr was dissolved in  $20 \text{ mL}$  of deionized water under continuous stirring until the solution became transparent. Subsequently, KBr was poured into the abovementioned solution. After stirring for  $5 \text{ h}$ , the suspension was filtered, repeatedly washed with deionized water and absolute ethanol, and finally dried at  $60^\circ\text{C}$  overnight.

**ACSs.** A three-necked flask was set in an oil bath, and  $200 \text{ mL}$  of deionized water was added to it. Then,  $30 \text{ mL}$  of *m*-cresol,  $33 \text{ mL}$  of formaldehyde,  $15 \text{ mL}$  of ethylene glycol and  $1.5 \text{ mL}$  of trimethylamine were successively added to the three-necked flask. After this,  $1.5 \text{ g}$  of polyvinyl alcohol and  $1.8 \text{ g}$  of hexamethylenetetramine were added under continuous stirring when the temperature increased to  $110^\circ\text{C}$ . After stirring for  $3 \text{ h}$ , the phenolic resin sphere samples were poured out, obtained,



heated at 850 °C under a N<sub>2</sub> atmosphere, and then activated by steam for 1 h to obtain ACSs.

**BiOBr/ACSs.** The BiOBr/ACSs samples were prepared by an impregnation method. Typically, 2 g of ACSs was added to a 0.05% polyvinyl alcohol solution and stirred for 1.5 h. The product was obtained by filtration. After this, 1 g of BiOBr was added to 20 mL of deionized water, the mixture was stirred for 10 min and ultrasonicated for 10 min, such that BiOBr was evenly dispersed in deionized water. The ACSs were added to the BiOBr solution and stirred for 20 min. After the reaction was completed, the product was filtered and dried at 60 °C for 12 h. The samples obtained were named BiOBr/ACSs, as shown in Scheme 1.

### 2.3 Characterization

The crystal phase of the as-prepared samples was investigated by X-ray diffraction (XRD) (DX-2700 diffractometer, Japan) with Cu K $\alpha$  radiation in the  $2\theta$  range of 10–80°. The morphologies and element mapping of the prepared samples were investigated *via* the Nanosem 430 (FEI, America) field emission scanning electron microscope at the operating voltage of 10 kV with an energy dispersive X-ray (EDX) microanalysis system. XPS spectra of these materials were obtained *via* Thermo Fisher ESCALAB 250 xi, England, using Al K $\alpha$  radiation (1486.6 eV). Binding energies were calculated with respect to C(1s) at 284.8 eV. Binding energies were measured with a precision of  $\pm 0.05$  eV. The UV-vis diffuse reflection spectra (UV-vis DRS) were obtained using a UV-vis spectrophotometer (UV-3600, Shimadzu, Japan). Photoluminescence (PL) spectra were obtained using the Hitachi F-7000 Fluorescence spectrophotometer. The specific surface area and porous structure of all the samples were determined by N<sub>2</sub> adsorption/desorption using the V-Sorb 4800P instrument. The CO<sub>2</sub> adsorption isotherm was obtained using an automated gas sorption analyzer (Quantachrome Autosorb-1, USA). Temperature-programmed desorption of CO<sub>2</sub> (CO<sub>2</sub>-TPD) was measured as follows: 0.1 g

of sample was pretreated at 400 °C for 1 h under a He atmosphere and then naturally cooled down to 30 °C. Next, the samples were placed under a CO<sub>2</sub> atmosphere for 0.5 h to ensure sufficient CO<sub>2</sub> adsorption. Before desorption, the sample was purged with He for 3 h and then desorbed at the rate of 10 °C min<sup>−1</sup> to 350 °C under a He atmosphere.

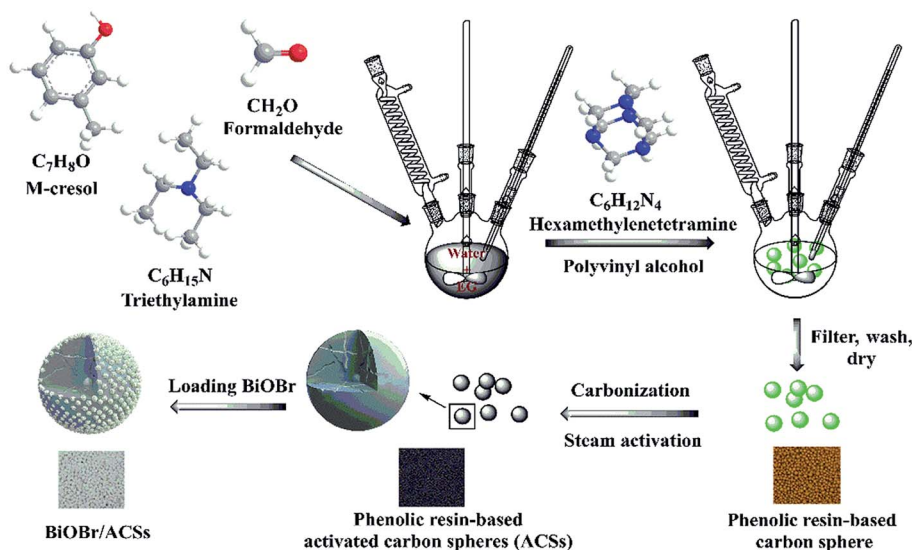
### 2.4 Photocatalytic CO<sub>2</sub> reduction

Photocatalytic CO<sub>2</sub> reduction experiments were carried out in a gas-closed circulation system (CEL-SPH2N-D9, Beijing China Education Au-Light Co., Ltd.) irradiated with a 300 W xenon lamp. Herein, 50 mL of deionized water was added to the quartz glass reactor, and a certain amount of catalyst was uniformly dispersed in the quartz glass reactor. Before turning on the light, the photoreactor system needed a thorough vacuum treatment, and CO<sub>2</sub> gas was introduced into the circulation system. During the light irradiation of 9 h, the yield of CO produced was analyzed every hour by on-line gas chromatography (GC-7920, Beijing China Education Au-Light Co., Ltd.) with a flame ionization detector. Gas products were analyzed by an external standard method.

## 3. Results and discussion

### 3.1 Phase structure analysis

Fig. 1 shows the XRD patterns of the as-prepared BiOBr, ACSs, and BiOBr/ACSs samples. The XRD peaks of the BiOBr sample are well indexed to the tetragonal phase BiOBr (JCPDF no. 73-348),<sup>13</sup> and no impurity peak is detected; this indicates high purity of as-prepared BiOBr sample. It has been found that the XRD patterns of BiOBr obtained after loading BiOBr onto ACSs do not shift significantly; this implies that the effect of ACSs on the phase structure of the BiOBr sample is negligible.



Scheme 1 Preparation process of BiOBr/ACSs.





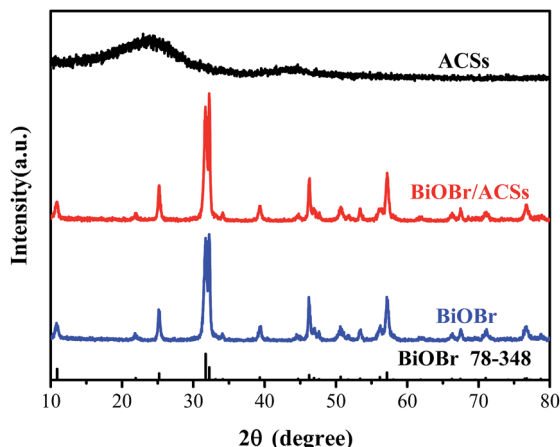


Fig. 1 XRD patterns of ACSs, BiOBr/ACSs and BiOBr samples.

### 3.2 Morphological structure and energy dispersive X-ray (EDX) analysis

Fig. 2 shows the SEM images of the prepared samples. In Fig. 2(a and b), it is found that the BiOBr sample exhibits a self-assembled sphere-structure with the single sphere diameter of approximately 0.8–1.2  $\mu\text{m}$ . Moreover, the surface of the ACSs activated by steam is smooth and free from cracks with good sphericity (Fig. 2c), and an excellent pore-structure distribution is obtained *via* the carbonization process (inset in upper-right corner of Fig. 2e); the abovementioned conditions are favorable for the activation agent to enter the interior of the sample during the activation process, and finally, the formation of ACSs with different, new and expanding pore-distributions is achieved. For the BiOBr/ACSs sample (Fig. 2d), a large amount of white BiOBr powder obviously adheres to the ACSs surface (Fig. S1†), and BiOBr loading has almost no influence on the internal pore-structure distribution of ACSs, as shown in the partially magnified half-section of BiOBr/ACSs (Fig. 2f). In the high-magnification SEM image of BiOBr/ACSs (Fig. S1†), we can observe that BiOBr supported on the surface of ACSs still maintains its self-assembled spherical nanosheet structure; this indicates that there is almost no change in the morphology of BiOBr and ACSs before and after loading.

To further clarify the chemical compositions of the samples, the corresponding energy dispersive X-ray spectroscopy (EDX) elemental mappings (Fig. 2g–h) and EDX spectra (Fig. S2†) of the C, O, Bi and Br (Fig. 2i–l) elements were obtained. The atomic ratio of the Bi, O and Br elements is very close to the reasonable value of 1 : 1 : 1, and the observed Bi, O and Br elemental mappings well indicate that BiOBr can be evenly distributed and wrapped on the ACSs surface; thus, the excellent BiOBr/ACSs catalyst system can be formed.

### 3.3 XPS spectra

To confirm the elemental compositions and valence states of the as-prepared samples, XPS survey spectra of the BiOBr sample were obtained, as shown in Fig. 3. It can be clearly seen from the wide survey scan data shown in Fig. 3a that Bi, O and Br are present without other prominent impurities; this rules out the possibility of the existence of adventitious carbon-based

contaminants, and this is in good agreement with the above-mentioned EDX scan results. The high-resolution XPS Bi 4f spectrum of BiOBr is presented in Fig. 3b. The two peaks at 164.5 and 159.2 eV are associated with Bi 4f<sub>5/2</sub> and Bi 4f<sub>7/2</sub>, respectively, indicating that the Bi<sup>3+</sup> valence state exists in the BiOBr nanosheets. As shown in Fig. 3d, the O 1s core level spectrum can be well fitted with the peak at 530.2 eV that belongs to the lattice oxygen O<sup>2-</sup> originating from the Bi–O bond.<sup>34</sup> The XPS spectrum of Br 3d (Fig. 3c) exhibits two major peaks with the binding energies at 68.4 and 69.4 eV, corresponding to Br 3d<sub>5/2</sub> and Br 3d<sub>3/2</sub> of Br<sup>-</sup>.

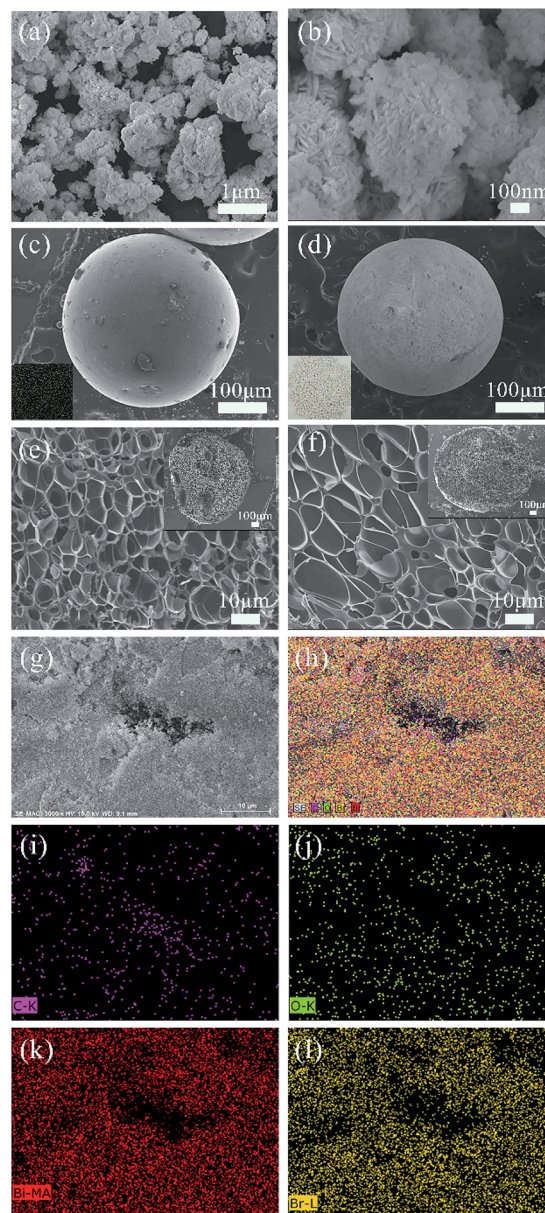


Fig. 2 Low (a) and high (b) magnification SEM images of BiOBr, low-magnification SEM images of ACSs (c) and BiOBr/ACSs (d) (inset c: an image of ACSs; inset d: an image of BiOBr/ACSs), a high-magnification SEM image of ACSs (e) and BiOBr/ACSs (f) cross profiles (inset: low-magnification SEM images of ACSs (e) and BiOBr/ACSs (f) cross profile); (g and h) EDX mappings of the BiOBr/ACSs samples, C (i), O (j), Bi (k), and Br (l) elements.



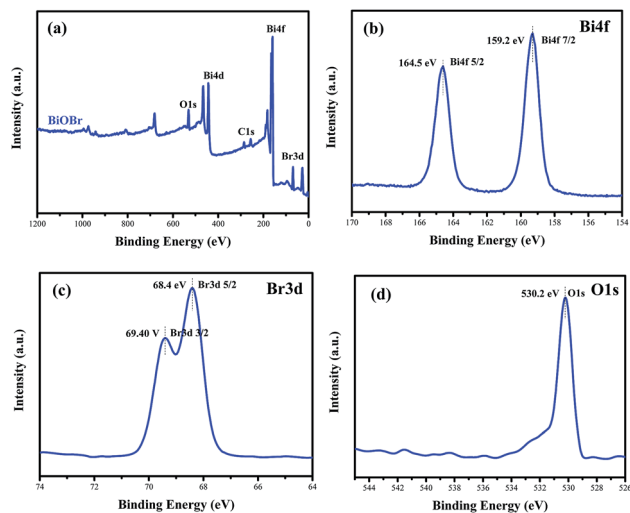


Fig. 3 Survey XPS spectra (a) and high-resolution XPS spectra of BiOBr: Bi 4f (b), Br 3d (c) and O 1s (d).

### 3.4 Optical absorption properties

The optical absorption properties of the samples were analyzed *via* the DRS technology and PL spectroscopy, as illustrated in Fig. 4. The band gap ( $E_g$ ) of BiOBr and BiOBr/ACSSs can be calculated by the equation  $(\alpha h\nu)n = A(h\nu - E_g)^{35,36}$ . Fig. 4c displays the curve of  $(\alpha h\nu)^{1/2}$  *vs.*  $h\nu$  according to the obtained BiOBr and BiOBr/ACSSs DRS spectra, and the extrapolation intercept provides the  $E_g$  values for BiOBr and BiOBr/ACSSs of 2.36 and 0.946 eV, respectively. After the introduction of ACSs, it can be clearly found that the BiOBr/ACSSs sample has stronger optical absorption in the visible region than pure BiOBr. Thus, the addition of ACSs could improve the visible light-driven efficiency of BiOBr, enhancing the photocatalytic activity of BiOBr. Moreover, for the photocatalytic  $\text{CO}_2$  reduction process, the separation efficiency of photo-generated carriers should be an important factor. Herein, the PL spectra were obtained to evaluate the separation efficiency of the photo-generated  $\text{e}^-$ - $\text{h}^+$  pairs for the BiOBr and BiOBr/ACSSs samples, as shown in Fig. 4b. As is known, the higher the PL intensity, the higher the probability of recombination of photo-generated  $\text{e}^-$ - $\text{h}^+$  pairs. It can be found that both pure BiOBr and BiOBr/ACSSs samples have a diffraction peak at 400 nm; however, the latter reveals decreased intensity when compared with the former; this confirms an improved separation efficiency of the  $\text{e}^-$ - $\text{h}^+$  pairs after the introduction of ACSs.<sup>37</sup> The EIS measurement results (Fig. S3†) reveal that the Nyquist circle of BiOBr/ACSSs is smaller than that of BiOBr; this indicates that BiOBr/ACSSs have lower resistance than pure BiOBr; this can accelerate the interfacial charge-transfer process.<sup>38</sup>

### 3.5 $\text{CO}_2$ adsorption performance and porous structure parameters

The  $\text{CO}_2$  adsorption performance of a catalyst has been considered as one of the most key factors influencing the catalytic activity in the photocatalytic  $\text{CO}_2$  reduction process.<sup>39</sup> The  $\text{CO}_2$  adsorption isotherms and  $\text{CO}_2$  temperature-

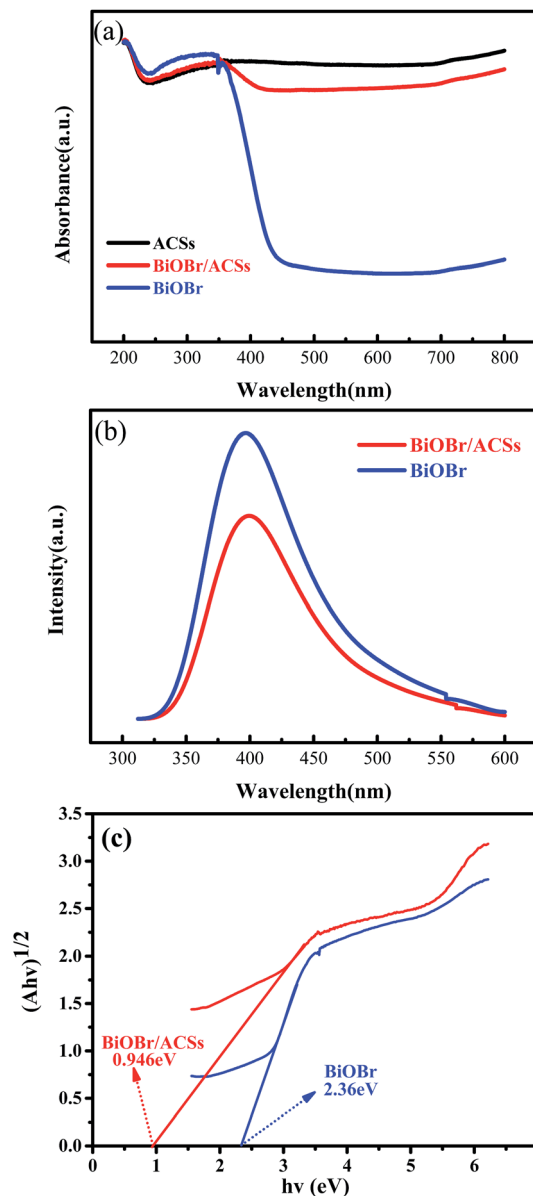


Fig. 4 (a) DRS of the as-prepared samples; (b) PL spectra of BiOBr and BiOBr/ACSSs samples; and (c) plots of  $(\alpha h\nu)^{1/2}$  versus photon energy ( $h\nu$ ).

programmed desorption ( $\text{CO}_2$ -TPD) spectra for the BiOBr, ACSs and BiOBr/ACSSs samples are provided in Fig. 5. The  $\text{CO}_2$  adsorption isotherms of the as-prepared sample at 298 K are shown in Fig. 5a. It is clearly seen that the  $\text{CO}_2$  adsorption capacity at 298 K over ACSs can reach  $10.03 \text{ mg g}^{-1}$ , much higher than that of BiOBr/ACSSs ( $7.0 \text{ mg g}^{-1}$ ) and BiOBr ( $2.23 \text{ mg g}^{-1}$ ); this should be ascribed to higher specific surface area and larger micropore volume of the ACSs and BiOBr/ACSSs. In Fig. 5b, it can be found that pure ACSs possess strongest  $\text{CO}_2$  adsorption capacity, and the desorption peaks of  $\text{CO}_2$  occur at  $50$ – $150^\circ\text{C}$  and  $260$ – $330^\circ\text{C}$ , which should be mainly attributed to strong physical adsorption and weak chemisorption, respectively.<sup>40,41</sup> In addition, pure BiOBr exhibits a notably weak  $\text{CO}_2$  desorption curve; however, after loading BiOBr on the ACSs surface, the intensity of the  $\text{CO}_2$  adsorption and desorption



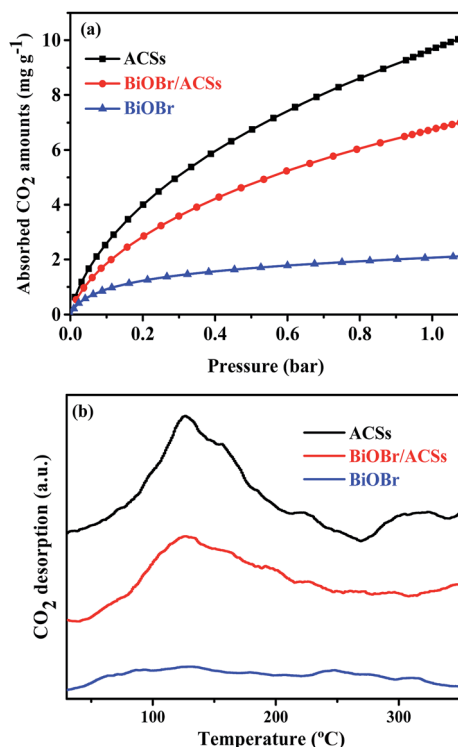


Fig. 5 (a)  $\text{CO}_2$  adsorption isotherms and (b)  $\text{CO}_2$  temperature-programmed desorption ( $\text{CO}_2$ -TPD) of the as-prepared samples.

curves of the BiOBr/ACSSs sample is obviously enhanced; this will be conducive to make an increasing number of  $\text{CO}_2$  molecules participate in the surface-activation and catalytic reaction process; this will improve the catalytic reaction efficiency and rate.<sup>42</sup>

Usually, a material with high surface area, large micropore volume and more basic surface functions should have higher  $\text{CO}_2$  capture performance.<sup>43,44</sup> Table 1 summarizes the corresponding structural parameters, including BET surface areas, average pore sizes, micropore and total pore volumes, as calculated from the  $\text{N}_2$  adsorption isotherms, of all the as-prepared samples. As can be observed from Table 1, the ACSs and BiOBr/ACSSs samples have rather the high specific BET surface areas of 936.42 and 792.56  $\text{m}^2 \text{g}^{-1}$ , total pore volumes of 0.37 and 0.31  $\text{cm}^3 \text{g}^{-1}$ , and a high micropore ratio (>83%), respectively. These higher micropore surface area and larger micropore volume can provide more physical activation sites for  $\text{CO}_2$  adsorption, and the kinetic diameter of  $\text{CO}_2$  is 0.33 nm such that the  $\text{CO}_2$  adsorption capacity should ultimately be controlled by the micropore volume.<sup>43,45</sup> These are the main reasons why ACSs exhibit higher  $\text{CO}_2$  adsorption ability than the BiOBr/ACSSs and BiOBr samples.

### 3.6 Photocatalytic $\text{CO}_2$ reduction

Fig. 6 shows the plots of a series of experiments for the photocatalytic  $\text{CO}_2$  reduction over ACSs, BiOBr/ACSSs and BiOBr samples under simulated sunlight irradiation. It can be found that  $\text{CO}_2$  cannot be reduced to CO in the absence of the BiOBr photocatalyst or in the dark during these controlled experiments. Only a small amount of CO gas was detected in the reaction system when BiOBr was used as a single photocatalyst under simulated sunlight irradiation (Fig. 6a). Surprisingly, the BiOBr/ACSSs sample exhibits significant photocatalytic  $\text{CO}_2$  reduction activity and has fast-raised CO gas production efficiency with an increase in the irradiation time, with the CO yield of 213.67  $\mu\text{mol g}^{-1}$  after 9 h, about 9.9 times that of pure BiOBr (21.51  $\mu\text{mol g}^{-1}$ ). For the BiOBr/ACSSs photocatalyst, the enhanced performance of photocatalytic  $\text{CO}_2$  reduction should mainly be related to the lower electron-hole charge recombination rate (Fig. 4b), higher micropore surface area (792.56  $\text{m}^2 \text{g}^{-1}$ ) and larger micropore volume that can provide more physical activation sites for  $\text{CO}_2$  adsorption (Fig. 5).

Furthermore, the relevant cyclic experiments (Fig. 6c) further reveal that the photocatalytic activity of the BiOBr/ACSSs sample only decreases about 8.28% after three cycles (9 h per cycle). Thus, our as-prepared BiOBr/ACSSs sample should exhibit high activity, stability and reusability for photocatalytic  $\text{CO}_2$  reduction.

### 3.7 Photocatalytic mechanism

Generally, the conduction band minimum (CBM) of a semiconductor decided its photocatalytic reduction ability, and a higher CBM will endow the semiconductor with better photocatalytic reduction ability.<sup>20</sup> Fig. 7 shows the valence band (VB) XPS spectra of the as-prepared BiOBr sample. It is found that the VB maximum of BiOBr is 1.81 eV. Combined with the DRS data of  $E_g$  (about 2.36 eV) for BiOBr, the calculated CBM should be  $-0.55$  eV (obtained using the equation  $E_{\text{CB}} = E_{\text{VB}} - E_g$ ),<sup>1</sup> higher than the  $E_0(\text{CO}_2/\text{CO})$  value of  $-0.53$  eV. This is the main reason why a certain photocatalytic  $\text{CO}_2$  reduction activity (2.39  $\mu\text{mol g}^{-1} \text{h}^{-1}$ ) of pure BiOBr exists.

Based on the abovementioned experimental results and theoretical analyses, a possible mechanism for the enhanced photocatalytic activity of BiOBr/ACSSs has been proposed in Scheme 2. As is known, the photocatalytic conversion of  $\text{CO}_2$  to CO should belong to a two-electron reduction reaction process at the gas-solid interface,<sup>4,46</sup> where  $\text{CO}_2$  adsorption on the catalyst surface and the efficient separation of photoinduced  $e^-$ - $h^+$  pairs are two rather important factors affecting the  $\text{CO}_2$  reduction reaction. At first, BiOBr/ACSSs can adsorb large amounts of  $\text{CO}_2$  when the system is filled with  $\text{CO}_2$  gas; this is mainly attributed to the contribution of a sufficient reaction

Table 1 Porous structure parameters of the as-prepared BiOBr, ACSs and BiOBr/ACSSs samples

Samples	$S_{\text{BET}}$ ( $\text{m}^2 \text{g}^{-1}$ )	$V_{\text{total}}$ ( $\text{cm}^3 \text{g}^{-1}$ )	$V_{\text{micro}}$ ( $\text{cm}^3 \text{g}^{-1}$ )	$V_{\text{semi}} - V_{\text{micro}}$ ( $\text{cm}^3 \text{g}^{-1}$ )	$D_p$ (nm)
ACSs	936.42	0.37	0.34	0.32	1.58
BiOBr/ACSSs	792.56	0.31	0.26	0.25	1.56
BiOBr	21.13	0.11	0.008	—	20.82





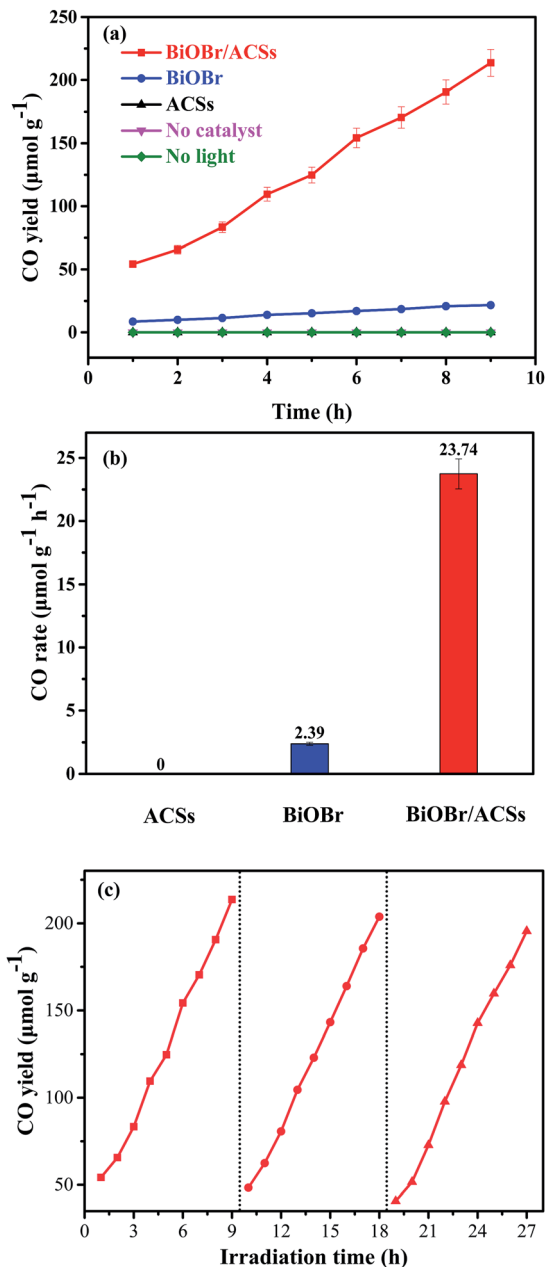


Fig. 6 Photocatalytic CO<sub>2</sub> reduction over BiOBr and BiOBr/ACSS samples under UV-vis irradiation: (a) CO yield, (b) CO rate and (c) cyclic experiments.

zone from ACSs with larger specific surface area and higher pore volume than that of pure BiOBr (Table 1); consequently, a higher number of CO<sub>2</sub> physical adsorption sites are achieved on the catalyst surface *via* the assistance of ACSs. Then, under simulated sunlight irradiation, BiOBr/ACSS have a more efficient e<sup>-</sup>-h<sup>+</sup> pair separation than BiOBr (as seen in Fig. 4b); this should be related to the intrinsic electron transport capacity of ACSs,<sup>47,48</sup> bringing about more efficient electron transfer to avoid the fast recombination of photoinduced electron-hole pairs. Finally, the valence band (VB) electrons (e<sup>-</sup>) of BiOBr are excited to its CBM, and CO<sub>2</sub> activation is achieved; moreover, the holes (h<sup>+</sup>) left in VBM react with H<sub>2</sub>O to provide H<sup>+</sup> (h<sup>+</sup> + H<sub>2</sub>O

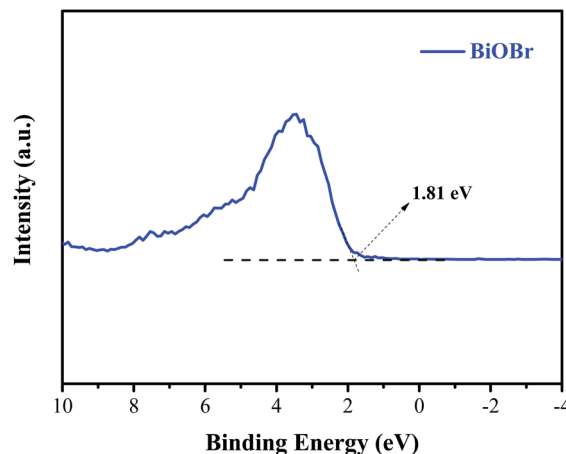
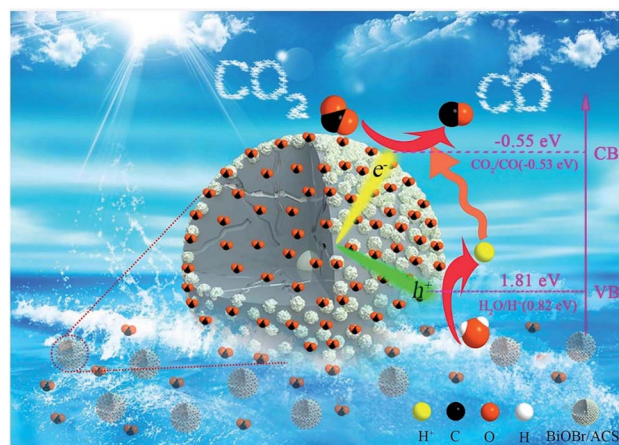


Fig. 7 Valence-band XPS spectra of BiOBr.



Scheme 2 Possible mechanism of the photocatalytic CO<sub>2</sub> reduction to CO over BiOBr/ACSS.

→ H<sup>+</sup> + 1/2O<sub>2</sub>) for the reduction of CO<sub>2</sub> to CO (2H<sup>+</sup> + CO<sub>2</sub> + 2e<sup>-</sup> → 2CO + H<sub>2</sub>O). Therefore, our findings on the enhanced photocatalytic CO<sub>2</sub> reduction activity of BiOBr assisted by ACSs should provide new ideas and an interesting guidance for the construction of high-efficiency photocatalyst systems in the field of CO<sub>2</sub> reduction to useful high-energy fuels.

## 4. Conclusions

In summary, phenolic resin spheres were prepared by suspension polymerization, and the ACSs were obtained *via* carbonization and steam activation; moreover, the BiOBr/ACSS photocatalyst was built using ACSs as a carrier. The photocatalytic results showed that BiOBr/ACSS had highest photocatalytic activity, with a yield of 213.67 μmol g<sup>-1</sup> after 9 hours, about 9.9 times that of BiOBr (21.51 μmol g<sup>-1</sup>), and a corresponding CO production rate of approximately 23.74 μmol g<sup>-1</sup> h<sup>-1</sup> and 2.39 μmol g<sup>-1</sup> h<sup>-1</sup>. Through the characterization of the prepared samples, we found that the following excellent characteristics of ACSs improved the ability of BiOBr to reduce CO<sub>2</sub>: (1) ACSs had no effect on the phase structure of BiOBr; (2) the



rich pore structure (>83% micropore ratio) and high specific surface area ( $936.42 \text{ m}^2 \text{ g}^{-1}$ ) of ACSs could provide more  $\text{CO}_2$  adsorption sites on the catalyst surface and adsorb more  $\text{CO}_2$  molecules ( $10.03 \text{ mg g}^{-1}$ ); this allowed BiOBr to be under a  $\text{CO}_2$ -enriched atmosphere; (3) the addition of ACSs could reduce the recombination rate of photo-generated electron-hole pairs, improving the effective electron mobility of BiOBr and thus enhancing the photocatalytic activity. Our findings should provide a new insight and method for the design and construction of highly active Bi-based photocatalytic materials assisted by ACSs.

## Conflicts of interest

There are no conflicts to declare.

## Acknowledgements

This work was supported by the National Natural Science Foundation of China (No. 21506144, 21676178, 21706179), the Natural Science Foundation of Shanxi Province (201701D221037, 201801D211008), and the Foundation of State Key Laboratory of Coal Conversion (J18-19-605). In addition, the author is particularly grateful to Dr Jinbo Xue for his guidance on the article.

## Notes and references

- 1 C. h. Ding, L. Q. Ye, Q. Zhao, Z. G. Zhong, K. C. Liu, H. Q. Xie, K. Y. Bao, X. G. Zhang and Z. X. Huang, *J. CO2 Util.*, 2016, **14**, 135–142.
- 2 G. Centi and S. Perathoner, *ChemSusChem*, 2010, **3**, 195–208.
- 3 E. J. Maginn, *J. Phys. Chem. Lett.*, 2010, **1**, 3478–3479.
- 4 S. N. Habisreutinger, L. Schmidt-Mende and J. K. Stolarczyk, *Angew. Chem., Int. Ed.*, 2013, **52**, 7372–7408.
- 5 S. Kamimura, Y. Sasaki, M. Kanaya, T. Tsubota and T. Ohno, *RSC Adv.*, 2016, **6**, 112594–112601.
- 6 J. Rosen, G. S. Hutchings, Q. Lu, S. Rivera, Y. Zhou, D. G. Vlachos and F. Jiao, *ACS Catal.*, 2015, **5**, 4293–4299.
- 7 E. E. Benson, C. P. Kubiak, A. J. Sathrum and J. M. Smieja, *Chem. Soc. Rev.*, 2009, **38**, 89–99.
- 8 M. Rakowski DuBois and D. L. DuBois, *Acc. Chem. Res.*, 2009, **42**, 1974–1982.
- 9 B. Kumar, M. Llorente, J. Froehlich, T. Dang, A. Sathrum and C. P. Kubiak, *Annu. Rev. Phys. Chem.*, 2012, **63**, 541–569.
- 10 C. Costentin, M. Robert and J. M. Saveant, *Chem. Soc. Rev.*, 2013, **42**, 2423–2436.
- 11 T. W. Woolerton, S. Sheard, E. Reisner, E. Pierce, S. W. Ragsdale and F. A. Armstrong, *J. Am. Chem. Soc.*, 2010, **132**, 2132–2133.
- 12 Y. Yang, C. Zhang, C. Lai, G. M. Zeng, D. L. Huang, M. Cheng, J. J. Wang, F. Chen, C. Y. Zhou and W. P. Xiong, *Adv. Colloid Interface Sci.*, 2018, **254**, 76–93.
- 13 M. Hu, R. Li, X. C. Zhang, C. M. Zhang, H. Zhang, C. M. Fan and J. Zhu, *RSC Adv.*, 2017, **7**, 50079–50086.
- 14 R. Li, X. Y. Gao, C. M. Fan, X. C. Zhang, Y. W. Wang and Y. F. Wang, *Appl. Surf. Sci.*, 2015, **355**, 1075–1082.
- 15 H. Tian, Y. Fan, Y. Zhao and L. Liu, *RSC Adv.*, 2014, **4**, 13061.
- 16 H. F. Cheng, B. B. Huang and Y. Dai, *Nanoscale*, 2014, **6**, 2009–2026.
- 17 H. P. Lin, W. W. Lee, S. T. Huang, L. W. Chen, T. W. Yeh, J. Y. Fu and C. C. Chen, *J. Mol. Catal. A: Chem.*, 2016, **417**, 168–183.
- 18 R. He, D. Xu, B. Cheng, J. Yu and W. Ho, *Nanoscale Horiz.*, 2018, **3**, 464–504.
- 19 L. Q. Ye, X. L. Jin, C. Liu, C. H. Ding, H. Q. Xie, K. H. Chu and P. K. Wong, *Appl. Catal., B*, 2016, **187**, 281–290.
- 20 D. Wu, L. Q. Ye, H. Y. Yip and P. K. Wong, *Catal. Sci. Technol.*, 2017, **7**, 265–271.
- 21 J. Wu, X. D. Li, W. Shi, P. Q. Ling, Y. F. Sun, X. C. Jiao, S. Gao, L. Liang, J. Q. Xu, W. S. Yan, C. M. Wang and Y. Xie, *Angew. Chem., Int. Ed.*, 2018, **57**, 8719–8723.
- 22 J. R. Ran, M. Jaroniec and S. Z. Qiao, *Adv. Mater.*, 2018, **30**, 1704649.
- 23 M. Q. Yang and Y. J. Xu, *Nanoscale Horiz.*, 2016, **1**, 185–200.
- 24 X. X. Chang, T. Wang and J. L. Gong, *Energy Environ. Sci.*, 2016, **9**, 2177–2196.
- 25 Y. Bai, L. Q. Ye, L. Wang, X. Shi, P. Q. Wang, W. Bai and P. K. Wong, *Appl. Catal., B*, 2016, **194**, 98–104.
- 26 Y. H. Ao, H. Tang, P. F. Wang, C. Wang, J. Hou and J. Qian, *Composites, Part B*, 2014, **59**, 96–100.
- 27 X. H. Xia, Z. J. Jia, Y. Yu, Y. Liang, Z. Wang and L. L. Ma, *Carbon*, 2007, **45**, 717–721.
- 28 Y. T. Liang, B. K. Vijayan, K. A. Gray and M. C. Hersam, *Nano Lett.*, 2011, **11**, 2865–2870.
- 29 B. Song, T. T. Wang, H. G. Sun, Q. Shao, J. K. Zhao, K. K. Song, L. H. Hao, L. Wang and Z. H. Guo, *Dalton Trans.*, 2017, **46**, 15769–15777.
- 30 Z. Yang, X. Hao, S. Chen, Z. Ma, W. Wang, C. Wang, L. Yue, H. Sun, Q. Shao, V. Murugadoss and Z. Guo, *J. Colloid Interface Sci.*, 2019, **533**, 13–23.
- 31 S. X. Liu, J. Sun and Z. H. Huang, *J. Hazard. Mater.*, 2010, **173**, 377–383.
- 32 N. P. Wickramaratne and M. Jaroniec, *ACS Appl. Mater. Interfaces*, 2013, **5**, 1849–1855.
- 33 R. Ocampo-Pérez, M. Sánchez-Polo, J. Rivera-Utrilla and R. Leyva-Ramos, *Appl. Catal., B*, 2011, **104**, 177–184.
- 34 X. C. Zhang, B. Q. Lu, R. Li, X. L. Li, X. Y. Gao and C. M. Fan, *Sep. Purif. Technol.*, 2015, **154**, 68–75.
- 35 E. A. Davis and N. F. Mott, *Philos. Mag.*, 1970, **22**, 0903–0922.
- 36 J. Tauc, R. Grigorovici and A. Vancu, *Phys. Status Solidi B*, 1966, **15**(2), 627–637.
- 37 C. Gao, S. M. Chen, Y. Wang, J. W. Wang, X. S. Zheng, J. F. Zhu, L. Song, W. K. Zhang and Y. J. Xiong, *Adv. Mater.*, 2018, **30**, 1704624.
- 38 J. Xia, J. Di, S. Yin, H. Xu, J. Zhang, Y. Xu, L. Xu, H. Li and M. Ji, *RSC Adv.*, 2014, **4**, 82–90.
- 39 J. Di, C. Zhu, M. Ji, M. Duan, R. Long, C. Yan, K. Gu, J. Xiong, Y. She, J. Xia, H. Li and Z. Liu, *Angew. Chem., Int. Ed.*, 2018, **57**, 14847–14851.
- 40 Y. L. Zhao, Y. C. Wei, X. X. Wu, H. L. Zheng, Z. Zhao, J. Liu and J. M. Li, *Appl. Catal., B*, 2018, **226**, 360–372.
- 41 Y. Bai, P. Yang, P. Q. Wang, H. Q. Xie, H. F. Dang and L. Q. Ye, *J. CO2 Util.*, 2018, **23**, 51–60.





- 42 H. Cheng, B. Huang, Y. Liu, Z. Wang, X. Qin, X. Zhang and Y. Dai, *Chem. Commun.*, 2012, **48**, 9729–9731.
- 43 C. M. Zhang, W. Song, Q. L. Ma, L. J. Xie, X. C. Zhang and H. Guo, *Energy Fuels*, 2016, **30**, 4181–4190.
- 44 C. M. Zhang, W. Song, G. H. Sun, L. Xie, J. L. Wang, K. X. Li, C. G. Sun, H. Liu, C. E. Snape and T. Drage, *Energy Fuels*, 2013, **27**, 4818–4823.
- 45 N. P. Wickramaratne and M. Jaroniec, *J. Mater. Chem. A*, 2013, **1**, 112–116.
- 46 E. Karamian and S. Sharifnia, *J. CO<sub>2</sub> Util.*, 2016, **16**, 194–203.
- 47 Y. P. Zhai, Y. Q. Dou, D. Y. Zhao, P. F. Fulvio, R. T. Mayes and S. Dai, *Adv. Mater.*, 2011, **23**, 4828–4850.
- 48 M. Li, S. S. Xiang, X. Q. Chang and C. S. Chang, *J. Solid State Electrochem.*, 2016, **21**, 485–494.

